High resolution 3-D imaging via multi-pass SAR

J.Homer, I.D.Longstaff, Z.She and D.Gray

Abstract: Spaceborne/airborne synthetic aperture radar (SAR) systems provide high resolution two-dimensional terrain imagery. The paper proposes a technique for combining multiple SAR images, acquired on flight paths slightly separated in the elevation direction, to generate high resolution three-dimensional imagery. The technique could be viewed as an extension to interferometric SAR (InSAR) in that it generates topographic imagery with an additional dimension of resolution. The 3-D multi-pass SAR imaging system is typically characterised by a relatively short ambiguity length in the elevation direction. To minimise the associated ambiguities we exploit the relative phase information within the set of images to track the terrain landscape. The SAR images are then coherently combined, via a nonuniform DFT, over a narrow (in elevation) volume centred on the 'dominant' terrain ground plane. The paper includes a detailed description of the technique, background theory, including achievable resolution, and the results of an experimental study.

1 Introduction

Spaceborne/airborne synthetic aperture radar (SAR) systems provide high resolution terrain imagery in the radar look or slant range $\vec{s}$ and flight path or azimuth $\vec{x}$ directions. The resolution in the $\vec{x}$ direction is achieved through the synthesis of an extended one-dimensional aperture in that direction. In this paper we examine the use of multiple SAR imaging flight paths, each slightly offset from the others in the elevation direction $\vec{n}$ (see Fig. 1), to synthesise a two-dimensional aperture in the plane normal to the $\vec{s}$ direction. The result is the ability to generate true three-dimensional imagery, which is characterised by an improved ground range resolution as compared to the corresponding single-pass two-dimensional SAR images.

The idea of coherently combining multi-pass SAR images to attain improved ground-range resolution has previously been proposed by Prati *et al.* in [1, 2]. Their work, however, generates only 2-D images. Our approach could be viewed as an extension of this method. We coherently combine the multiple single-look complex (SLC) SAR images over a 3-D volume rather than over a 2-D surface. Alternatively, our procedure could be considered as an extension to interferometric SAR (InSAR) [2–7], which combines two SLC-SAR images to generate a topographic surface in 3-D space. Like other proposed extensions to standard 2-pass InSAR, such as those of [8, 9], our method provides a noise reduced topographic surface and minimises the need for phase unwrapping. However, unlike these other extensions, our method provides a third dimension of resolution.

A related technique for generating 3-D SAR imagery has been previously proposed in [10]. This technique, however, requires a linear array mounted in the elevation direction on a single aircraft/spacecraft. In practice, the $\vec{n}$ length of this fixed array is limited to several metres, as compared to several hundreds/thousands of metres for our $\vec{n}$ synthesised array. Our technique, consequently, has considerably better resolving power in the $\vec{n}$ direction.

The synthesis of our extended $\vec{n}$ aperture from sparsely separated flight paths also leads to a significantly different 3-D imaging procedure from that of [10]. In particular, the sparsely sampled $\vec{n}$ aperture results in a relatively short ambiguity length l_n in the elevation $\vec{n}$ direction. To minimise the associated imaging ambiguities [Note 1] we include a terrain landscape tracking stage within the procedure. Coherent summing of the SLC-SAR images then occurs only over a 'narrow' (in elevation) volume centred on the 'dominant' terrain ground plane.

2 Theory

2.1 Terminology

Consider the multi-pass imaging configuration shown in Fig. 1*a*, which shows N flight paths P_i, $i=1, 2, \ldots, N$,

IEE Proceedings online no. 20020059

DOI: 10.1049/ip-rsn:20020059

Paper first received 3rd February 2000 and in revised form 17th September 2001

J. Homer and I.D. Longstaff are with the School of Computer Science and Electrical Engineering, Cooperative Research Centre for Sensor Signal and Information Processing, The University of Queensland, Brisbane, Qld 4072, Australia

Z. She is with the School of Informatics, The University of Wales, Bangor, Gwynedd LL57 1UT, UK

D. Gray is with the Cooperative Research Centre for Sensor Signal and Information Processing, Department of Electrical and Electronic Engineering, The University of Adelaide, Adelaide, SA 5005, Australia

Note 1: That is, the occurrence of a 'ghost' image, which is separated from the 'real' image by the distance l_n in the elevation direction.

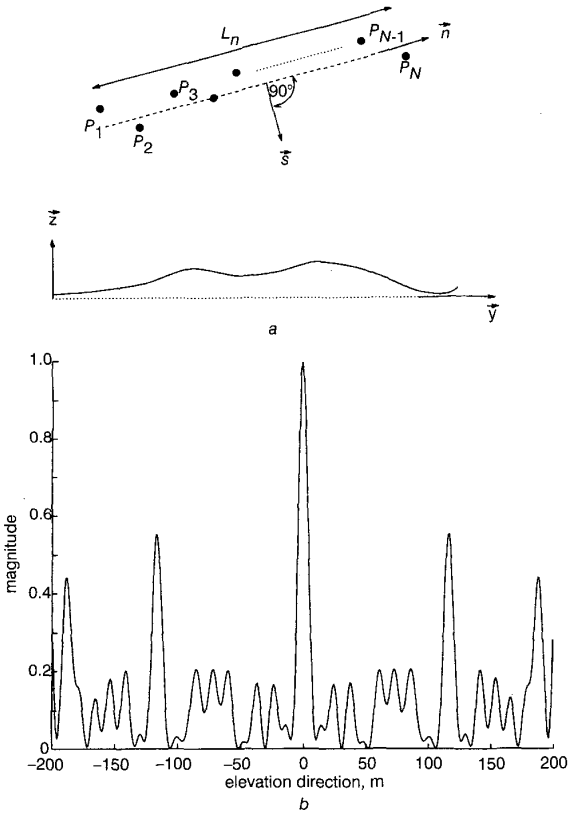

Fig. 1 *Proposed configuration for 3-D multi-pass SAR and beam pattern in elevation $\vec{n}$ direction*

a Proposed configuration for 3-D multi-pass SAR: a series of flight paths imaging the same terrain, each slightly separated from the others in the elevation $\vec{n}$ direction. The flight paths are directed into the page

b Beam pattern in $\vec{n}$ direction synthesised by set of flight paths considered in Section 4

directed into the page (the azimuth direction $\vec{x}$ is normal to the page). Assume the acquired SLC-SAR data sets $F_i(k, l)$ are co-registered so that a point on the terrain corresponds to the same pixel co-ordinates (k, l) in all data sets. Denote:

$s_i(k, l)$	slant-range of terrain corresponding to pixel (k, l) relative to flight path P_i
$x(k, l)$	azimuthal distance of pixel (k, l) from a ground based reference point T_{ref}
$y(k, l)$	ground-range of pixel (k, l) relative to a ground based reference point T_{ref}
$z(k, l)$	height of pixel (k, l) relative to T_{ref}
$n(k, l)$	elevation of pixel (k, l) relative to T_{ref}
$\phi_i(k, l)$	phase of pixel (k, l) of data set i
$\theta_i(k, l)$	radar look angle of pixel (k, l) from flight path P_i
B_i	baseline between flight paths P_i and P_{i+1}
$B_{n,i}$	component of B_i in elevation direction $\vec{n}$
λ	radar wavelength
$\theta(k, l)$	$\text{mean}_i[\theta_i(k, l)]$
$s(k, l)$	$\text{mean}_i[s_i(k, l)]$.

2.2 Elevation resolution

The Rayleigh resolution ρ_n which we achieve in the $\vec{n}$ direction is [11]

$$\rho_n = \frac{s\lambda}{2L_n} \tag{1}$$

where

$$L_n = \sum_{i=1}^{N-1} B_{n,i} \tag{2}$$

is the length in the $\vec{n}$ direction of the synthesised 2-D aperture.

2.3 Improved ground-range resolution

For a given local terrain region, a SAR imaging system with a radar look angle θ, radar bandwidth W and carrier frequency $f_c = c/\lambda$ samples a particular band of the wavenumber spectrum [1, 2], centred on

$$k_y = \frac{4\pi f_c \sin(\theta - \alpha_y)}{c \cos \alpha_y}$$

and having a width of

$$\delta_f k_y = \frac{4\pi W \sin(\theta - \alpha_y)}{c \cos \alpha_y}$$

where α_y is the angle the terrain makes with the horizontal in the ground-range direction. The ground-range resolution of the image is

$$\rho_{y,single} = \frac{2\pi}{\delta_f k_y} = \frac{\rho_s \cos \alpha_y}{\sin(\theta - \alpha_y)}$$

where $\rho_s = c/(2W)$ is the slant-range resolution.

For the proposed multi-pass SAR imaging system, which has an elevation angle span of $\Delta\theta = L_n/s$, the total wavenumber bandwidth is

$$\delta k_y = \delta_f k_y + \delta_\theta k_y$$

where

$$\delta_\theta k_y = \frac{4\pi \cos(\theta - \alpha_y) L_n}{s\lambda \cos \alpha_y}$$

Thus the improvement in ground range resolution is

$$\rho_{y,single}/\rho_{y,multi} = 1 + L_n/B_{crit} \tag{3}$$

where

$$B_{crit} = \frac{\lambda s \tan(\theta - \alpha_y)}{2\rho_s} \tag{4}$$

B_{crit} here corresponds to the upper limit on the baseline normal B_n in standard 2-pass interferometric SAR [2, 6, 7]. Note, to ensure the applicability of the DFT procedure described in the next section, we require that adjacent flight paths satisfy

$$B_{n,i} < B_{crit} \tag{5}$$

that is the corresponding single-pass wavenumber bands overlap.

3 Method

3.1 Preliminaries

Consider N SLC-SAR images acquired from N flight paths. Let the flight paths be indexed as indicated in Fig. 1*a*. We assume the temporal decorrelation amongst the images is relatively small and the $\vec{n}$ baselines $B_{n,i}$ between adjacent

flight paths P_i, P_{i+1} satisfy $B_{n,i} < B_{crit}$. We also assume the N SAR images have been accurately co-registered using, for example, the technique outlined in [6]. The 3-D multi-pass SAR procedure we propose involves firstly dividing the imaged region into localised subregions $\Re$. Subregion sizes similar to those used in the estimation of the local coherency of SAR image pairs, e.g. 16×4 [6], 20×5 [12] (azimuth, slant-range), should be suitable. For mosaicing purposes, neighbouring localised subregions need only overlap by one row or column. The procedural steps described below rely on the following additional (typically valid) assumptions: the slant-range distance s_i to the centre of each subregion $\Re$ is much greater than: (A1) the synthesised $\vec{n}$ aperture length L_n; (A2) the distance in the $\vec{s}$ direction spanned by the N flight paths; and (A3) the size of each subregion.

3.2 Landscape tracking

The susceptibility to $\vec{n}$ direction imaging ambiguities arises from the $\vec{n}$ direction synthesised aperture being a sampled rather than a continuous aperture. In particular, the synthesised beam pattern typically shows large grating-like lobes, as is evident in Fig. 1*b* at $n \approx \pm 120$ m. This distance between the first grating lobe and the main lobe of the $\vec{n}$ beam pattern is essentially the ambiguity length l_n in the $\vec{n}$ direction. Consequently, we need to coherently combine (see Section 3.3) each set of subimages over a narrow volume which is centred on the local dominant ground plane and no greater than l_n in elevation. This, in turn, requires the subimages to be initially phase aligned on this dominant plane. Note, that the distance l_n can be predetermined by simulating the $\vec{n}$ beam pattern from the set of baseline $B_{n,i}$ values.

Location of the 'local' dominant ground plane is achieved by exploiting a relationship between the terrain topography and the relative phase information within the set of SAR images. (This relationship is also the basis of interferometric SAR.) In particular, consider two SAR images F_i, F_j, the associated interferogram $F_iF_j^*$ and a subregion $\Re$ within this interferogram. Assume that the corresponding terrain subregion $\Re$ has a dominant ground plane slope of α_y and α_x in the ground-range $\vec{y}$ and azimuth $\vec{x}$ directions, respectively. The subregion of the interferogram then shows dominant phase gradients in the slant-range and azimuth directions of the interferogram [7]. We denote these dominant phase gradients by $\bar{\phi}'_{i,j,s}$, $\bar{\phi}'_{i,j,x}$, which under noise free conditions are given by:

$$\bar{\phi}'_{i,j,s} = \frac{4\pi B_{i,j,n}}{\lambda s \tan(\theta - \alpha_y)} \tag{6}$$

$$\bar{\phi}'_{i,j,x} = \frac{4\pi B_{i,j,n} \cos\alpha_y \tan\alpha_x}{\lambda s \sin(\theta - \alpha_y)} \tag{7}$$

where $B_{i,j,n}$ is the $\vec{n}$ baseline corresponding to the image pair F_i, F_j.

Phase alignment of the N subimages on the dominant ground plane is achieved by: (i) determining the local dominant $\vec{s}$ and $\vec{x}$ phase gradients $\bar{\phi}'_{i,1,s}$, $\bar{\phi}'_{i,1,x}$ and the phase offset $\bar{\phi}_{i,1,0}$ within each subimage relative to subimage F_1 (see Fig. 2 for an illustration of the above terms); (ii) removing these relative phase gradients and phase offsets from the corresponding subimages.

Substep (i) is carried out by applying a 2-D DFT to the interferograms generated from subimage pairs corresponding to adjacent flight paths. Then, for example, the set of slant range dominant phase gradients $\{\bar{\phi}'_{m,m+1,s}\}_{m=1}^{N-1}$ is

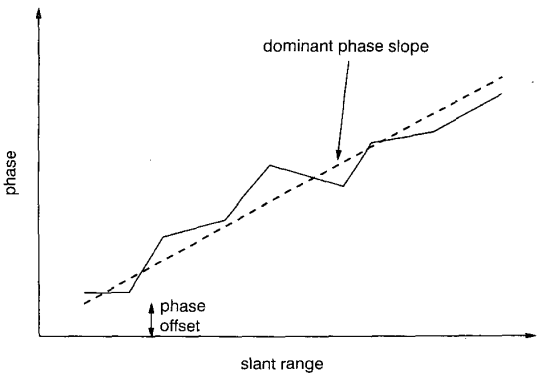

Fig. 2 *Illustrative example: variation in phase along slant direction within a subregion $\Re$ of an interferogram $F_iF_j^*$*

The dominant phase slope and the corresponding phase offset are indicated

determined and subsequently $\bar{\phi}'_{i,1,s} = \sum_{m=1}^{i-1} \bar{\phi}'_{m,m+1,s}$. (Note, we have assumed earlier that 'adjacent' subimage pairs are sufficiently coherent.)

3.3 Coherent summing via nonuniform DFT

Having phase aligned the images on the dominant ground plane, we now coherently combine them over a narrow (in elevation) volume. This is achieved via a nonuniform DFT as described below.

To image a scattering source located within the $\vec{s}$, $\vec{x}$ cell (k, l) and δn metres in the $\vec{n}$ direction off the dominant ground plane (see Fig. 3) we need to apply phase rotations $\Delta\phi_i$ to the phase aligned images $\bar{F}_i(k, l)$, where

$$\Delta\phi_i = \frac{4\pi B_{n,1,i+1}\delta n}{\lambda s_i} \tag{8}$$

where $B_{n,1,i+1}$ is the $\vec{n}$ baseline of flight paths P_1 and P_{i+1} and $B_{n,1,1} = 0$.

Due to finite resolution in the $\vec{n}$ direction, we only need to sample in this direction using an interval or cell size of

$$\Delta n \leq \rho_n = s_i\lambda/(2L_n)$$

Thus, imaging of the $\vec{n}$ distributed scattering sources within the $\vec{s}$, $\vec{x}$ cell indexed by (k, l) can be achieved by applying the following 'nonuniform' DFT based summation

$$G_t(k, l) = \sum_{i=1}^{N} \bar{F}_i(k, l) \exp\left(\frac{j2\pi B_{n,1,i+1} t}{pL_n}\right) \tag{9}$$

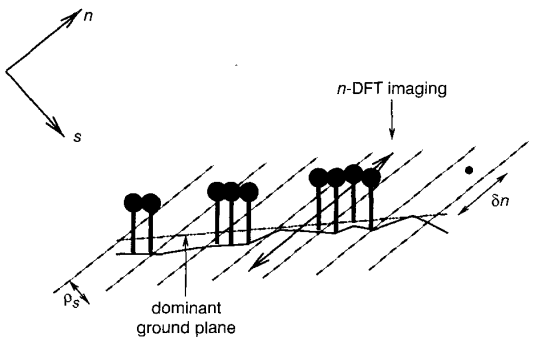

Fig. 3 *Illustrative example: images $\bar{F}_i(k, l)$ are phase aligned on dominant ground plane*

The summation, $G_{t=0}(k, l)$ of (9), corresponds to an image of dominant ground plane. Focused imaging of scatterers above and below this plane is achieved via application of full DFT based summation of (9)

where t is the cell index for the $\vec{n}$ direction and $p \geq 1$ is an $\vec{n}$ interpolation factor. For an $\vec{n}$ imaging ambiguity length of l_n we require $l_n p/\rho_n \geq t \geq l_n p/\rho_n$. To reiterate: the value of $|G_t(k, l)|$ indicates the backscattering strength of sources located in the 3-D $\vec{s} - \vec{x} - \vec{n}$ cell indexed by (k, l, t). Furthermore, the dominant ground plane image $G_{t=0}(k, l)$ is characterised by an improved ground range resolution according to (3).

3.4 Terrain slope estimation

The final step in the 3-D imaging of the subregion $\Re$ involves estimating the local dominant terrain slopes α_x, α_y and subsequently rotating the 3-D image accordingly. Estimates of α_x, α_y are obtained via the following equations, which are derived from (6) and (7):

$$\hat{\alpha}_y = \theta - \cot^{-1} Q \tag{10}$$

$$\hat{\alpha}_x = \tan^{-1} P \tag{11}$$

where

$$Q = \frac{\lambda s \bar{\phi}'_{i,j,s}}{4\pi B_{i,j,n}} \tag{12}$$

$$P = \frac{\lambda s \bar{\phi}'_{i,j,x} \sin(\theta - \hat{\alpha}_y)}{4\pi B_{i,j,n} \cos \hat{\alpha}_y} \tag{13}$$

With N multi-pass SAR images available, an estimate of the local dominant terrain slopes α_x, α_y is obtainable from each of the $N(N-1)/2$ SAR image pairs. A final estimate may then be obtained by taking a weighted average where the weighting is based on the coherency of the corresponding image pair.

3.5 Mosaicing of subregions

Consider two neighbouring subimage regions which overlap by one row of pixels:

$$\Re_1: (k_0 + k, l_0 + l)_{k,l=0}^{N,M}, \quad \Re_2: (k_0 + k, l_0 + M + l)_{k,l=0}^{N,M}$$

The dominant ground plane in $\Re_2$, in comparison to that in $\Re_1$, may not only have different slopes α_x, α_y but also be translated in the $\vec{n}$ direction. Mosaicing of the 3-D images of $\Re_1$ and $\Re_2$ is achieved by the following:

(a) Having already applied the procedure as outlined in Sections 3.2–3.4 to the subimages of $\Re_1$, ensure that the first pixel $F_i(k_0, l_0 + M)$ in each of the subimages of $\Re_2$ is phase aligned on the dominant ground plane identified in $\Re_1$.

(b) Apply the procedure, as outlined in Sections 3.2–3.4 to the resulting subimages of $\Re_2$. Use the determined phase offsets $\bar{\phi}_{i,1,0}$ to translate the 3-D subimage of $\Re_2$ by the following distance δn in the $\vec{n}$ direction (based on eqn. 8):

$$\delta n = \frac{1}{N-1} \sum_{i=1}^{N-1} \frac{\lambda s_i \bar{\phi}_{i+1,1,0}}{4\pi B_{n,1,i+1}} \tag{14}$$

Note that, in general, prior to determining the phase offsets relative to the first subimage, $\bar{\phi}_{i,1,0}$, the individual phase offsets $\bar{\phi}_{m,m+1,0}$ need to be phase unwrapped, that is

$$\bar{\phi}_{m,m+1,0} \rightarrow \phi_{m,m+1,0} + 2k\pi$$

where $k =$ integer is to be determined. This should be achieved easily as long as one of the image pairs is highly coherent; the phase offsets corresponding to this highly coherent image pair being used to guide the phase unwrapping of the less coherent image pairs.

4 Results

Nine SLC-SAR image data sets, acquired by the ERS-1 satellite over Bonn, Germany, during the period of 2–29 March 1992, were employed to demonstrate the proposed 3-D multi-pass SAR technique. Unfortunately, ground truthed data was not available for these data sets. Nevertheless, demonstration of the 3-D imaging capability was possible due to the presence of radar corner reflectors within the imaged terrain region.

The nine flight paths corresponding to the images provide an $\vec{n}$ synthesised aperture length of $L_n = 1686$ m. This, together with the following typical imaging parameter values of ERS-1: $\lambda = 0.0567$ m, $s = 800\,000$ m, $W = 15.55$ MHz, $\theta = 23°$, leads to an $\vec{s}$ resolution cell size of $\rho_s = 9.65$ m, an $\vec{n}$ resolution cell size of $\rho_n = 13.5$ m, a single-pass and an N-pass SAR image ground-range resolution (corresponding to flat terrain $\alpha_y = 0$) of $\rho_{y,single} = 24.7$ m and $\rho_{y,multi} = 9.17$ m, respectively, and a ground-range resolution enhancement of $\rho_{y,single}/\rho_{y,multi} \approx 2.7$. The synthesised beam-pattern for the set of flight paths is shown in Fig. 1*a*.

The multi-pass SAR procedure was applied to a region within the SAR images which consisted of 10 pixels in both the azimuth direction $\vec{x}$ and slant-range direction $\vec{s}$. The pixel spacings were $\Delta x = 4.0$ m, $\Delta s = 7.9$ m. We denote the region by $\Re$. A corner reflector was located near the centre of $\Re$. Fig. 4 includes a 500 by 500 pixel section of one of the SAR images, with the corner reflector of interest indicated.

Interpolation by a factor of 4, 8 was applied in the $\vec{x}$, $\vec{s}$ directions, respectively. In applying the multi-pass SAR procedure we employed an interpolation factor of $p = 3$ in the $\vec{n}$ direction. The pixel spacings in the resulting 3-D image $G^2(s, x, n)$ were then $\Delta s_G = 0.9875$ m, $\Delta x_G = 1.0$ m, $\Delta n_G = 4.5$ m.

Figures 5–8 include various displays of the generated 3-D intensity image $|G(s, x, n)|^2$. Fig. 5 is a surface contour plot with horizontal right hand axis corresponding to $\vec{x}$, horizontal left hand axis corresponding to $\vec{s}$ and the vertical axis to $\vec{n}$. For reasons of clarity, only the following section

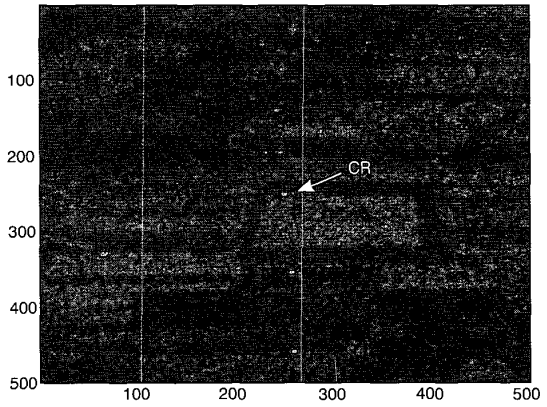

Fig. 4 *500 by 500 pixel section of one of the SAR images*
Corner reflector (CR) indicated is that which lies near the centre of the 10 by 10 pixel test region

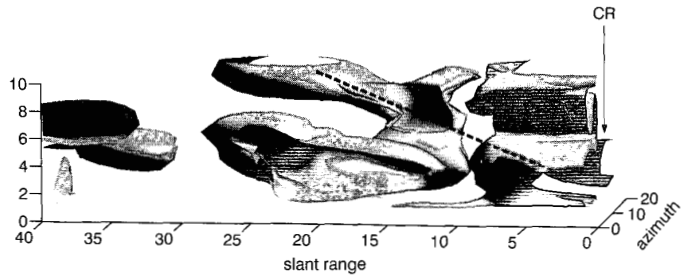

Fig. 5 *Surface contour image of section of multi-pass SAR image generated from series of SLC-SAR images considered in Section 4*

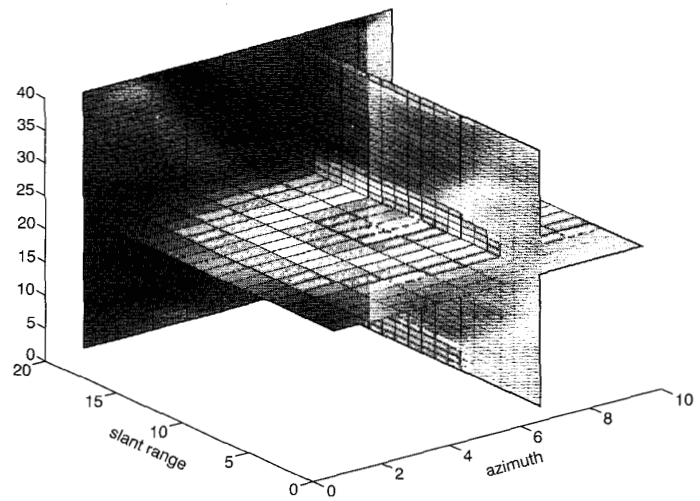

Fig. 6 *Slice diagram of section of multi-pass SAR image generated from series of SLC-SAR images considered in Section 4*

of the image is displayed, where (s_{CR}, x_{CR}, n_{CR}) are the co-ordinates of the corner reflector:

$$s_{CR} \le s \le s_{CR} + 39\Delta s_G, x_{CR} - 15\Delta x_G \le x \le x_{CR} + 4\Delta x_G, n_{CR} - \Delta n_G \le n \le n_{CR} + 8\Delta n_G$$

Fig. 5 includes two contour surfaces. The dark, light surface corresponds to $|G(s, x, n)|^2 = 2 \times 10^7, 2 \times 10^5$, respectively. The dark surface is associated with the corner reflector. The light surface is associated with the surrounding terrain. The dashed line indicates the location of the expected ground plane. Importantly, the dashed line appears to correspond to a dominant plane on the light contour surface.

Fig. 6 displays a 'slice' diagram of the image section:

$$s_{CR} - 9\Delta s_G \le s \le s_{CR} + 10\Delta s_G,$$
$$x_{CR} - 6\Delta x_G \le x \le x_{CR} + 3\Delta x_G,$$
$$n_{CR} - 5\Delta n_G \le n \le n_{CR} + 4.5\Delta n_G$$

Note: to improve the clarity of Fig. 6, the 3-D image $G(s, x, n)$ was interpolated by an additional factor of 2 in the $\vec{n}$ direction; that is, in Fig. 6 the $\vec{n}$ pixel spacing $\Delta n_G = 2.25$ m. Fig. 6 demonstrates clearly the 3-D resolving capability of the multi-pass SAR technique.

Figures 7 and 8 correspond to the image section:

$$s_{CR} - 27\Delta s_G \le s \le s_{CR} + 29\Delta s_G, x = x_{CR},$$
$$n_{CR} - 13.5\Delta n_G \le n \le n_{CR} + 14.5\Delta n_G$$

Note that this section is actually a slice in the $\vec{s}$, $\vec{n}$ plane centred on the CR. The pixel spacings in these two figures are the same as those in Fig. 6.

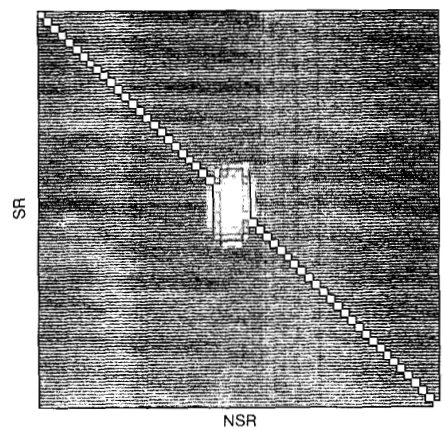

Fig. 7 *Grey scale multi-pass SAR image generated from series of SLC-SAR images considered in Section 4*
SR = slant-range direction; NSR = elevation direction

Fig. 7 is a grey scale image. The highlighted diagonal in the image, which has been artificially superimposed on the image, corresponds closely to the zeroth DFT component, that is to the dominant ground plane. Fig. 8*a* shows the corresponding mesh plot of $|G(s, x, n)|^2$. A close examination of Fig. 8*a*, and taking into account the pixel sizes, indicates that the Rayleigh resolution in each of these directions is close to the theoretical values of ρ_s, $\rho_n = 9.65$ m, 13.5 m, respectively.

Fig. 8*b* shows a plot of the pixel intensities $|G(s, x, n)|^2$ along the dominant ground plane, that is along the high-

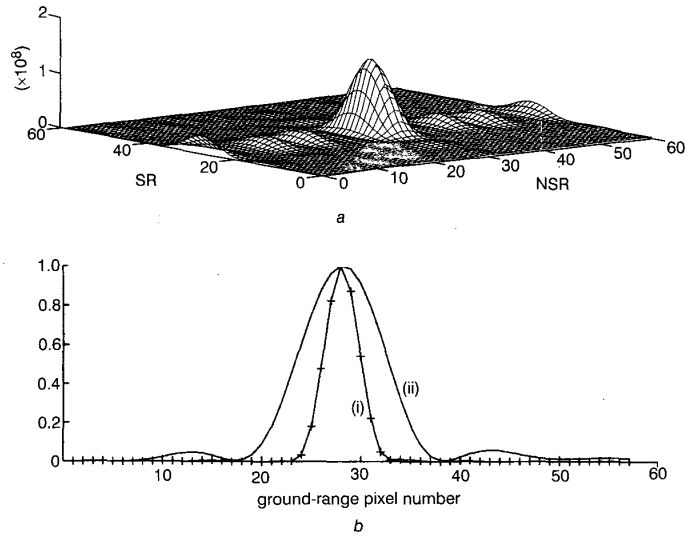

Fig. 8 *Intensity mesh plot corresponding to Fig. 7, and intensity plots along dominant ground plane*

a Intensity mesh plot
b Intensity plots along dominant ground plane, corresponding to highlighted diagonal in Fig. 7
(i) Pixel intensities of 3-D multi-pass image
(ii) Pixel intensities of single-pass SAR image

lighted diagonal in Fig. 7. This plot is essentially the response of the corner reflector in the ground-range direction and enables measurement of the ground range resolution achieved for this specific application of the 3-D multi-pass SAR technique. Included also in Fig. 8*b* is the corresponding intensity plot for one of the single-pass SAR images F_i. This latter plot was generated by projecting the single-pass SAR image intensity plot for region $\Re$ onto the dominant ground plane via $y(k, l) = s(k, l)/\sin\theta$. (Note: for the region, $\alpha_y \approx 0$.) A comparison of the half-power widths of the two plots indicates that the multi-pass SAR image has ~ 2.7 times better ground range resolution than the single-pass SAR image, which is in good agreement with the theoretical value.

5 Conclusion

In this paper we have examined the use of multiple single-look complex (SLC) SAR images, acquired on slightly separated flight paths, to generate 3-D imagery. The proposed technique essentially uses the flight paths to synthesise an aperture in the elevation $\vec{n}$ direction. This provides resolving power in the $\vec{n}$ direction, in addition to the slant-range and azimuth resolving power of SAR imagery. This additional dimension of resolution also leads to an improved ground-range resolution. The technique could be viewed as an extension to interferometric SAR (InSAR): the 3-D multi-pass SAR method generates topographic imagery with an additional dimension of resolution. Additional benefits over standard InSAR are a noise reduced topographic surface and considerable simplification of the difficult InSAR phase unwrapping step.

Imaging in the $\vec{n}$ direction (for a given local region) is achieved via: (i) phase alignment of the SAR images on the dominant ground plane; (ii) application of a nonuniform DFT to the set of phase aligned SAR images. The result is a 3-D image of the local region. The DFT parameters are determined by the flight path baselines. This procedure is repeated for all local regions within the imaged scene.

The 3-D imaging capabilities of the technique were demonstrated with a series of ERS-1 repeat-pass SAR images.

6 Acknowledgments

We would like to thank Dr Thiel from Institut fur Navigation, Universitat Stuttgart, as well as the European Space Agency for the provision of the ERS-1 data sets used in the experimental study.

7 References

1 PRATI, C., and ROCCA, F.: 'Improving slant-range resolution with multiple SAR surveys', *IEEE Trans. Aerosp. Electron. Syst.*, 1993, **29**, pp. 135–143
2 GATELLI, F., MONTI GUARNIERI, A., PARIZZI, F., PASQUALI, P., PRATI, C., and ROCCA, F.: 'The wavenumber shift in SAR interferometry', *IEEE Trans. Geosci. Remote Sens.*, 1994, **32**, pp. 855–865
3 GRAHAM, L.C.: 'Synthetic interferometer radar for topographic mapping', *Proc. IEEE*, 1974, **62**, (6), pp. 763–768
4 GABRIEL, A., and GOLDSTEIN, R.M.: 'Crossed orbit interferometry: theory and experimental results from SIR-B', *Int. J. Remote Sens.*, 1988, **9**, (5), pp. 857–872
5 MADSEN, S., and ZEBKER, H.: 'Topographic mapping using radar interferometry: processing techniques', *IEEE Trans. Geosci. Remote Sens.*, 1993, **31**, pp. 246–255
6 PRATI, C., ROCCA, F., MONTI GUARNIERI, A., and PASQUALI, P.: 'Report on ERS-1 SAR interferometric techniques and applications'. ESA Technical Report, Dip. di Elet., Politecnico di Milano, Milano, Italy, 1994
7 RODRIGUEZ, E., and MARTIN, J.M.: 'Theory and design of interferometric synthetic aperture radars', *IEE Proc. F*, 1992, **139**, (2), pp. 147–159
8 FERRETTI, A., MONTI GUARNIERI, A., PRATI, C., and ROCCA, F.: 'Multi baseline interferometric techniques and applications'. Proceedings of FRINGE96—ESA Workshop on Applications of ERS SAR Interferometry, Zurich, Switzerland, October 1996
9 MASSONET, D., VADON, H., and ROSSI, M.: 'Reduction of the need for phase unwrapping in radar interferometry', *IEEE Trans. Geosci. Remote Sens.*, 1996, **34**, pp. 489–497
10 MAHAFZA, B.R., and SAJJADI, M.: 'Three dimensional SAR imaging using linear array in transverse motion', *IEEE Trans. Aerosp. Electron. Syst.*, 1996, **32**, pp. 499–510
11 WEHNER, D.: 'High-resolution radar' (Artech House, Norwood, MA, 1995)
12 KOSKINEN, J.: 'The ISAR-Interferogram Generator Manual'. ESA Software User Manual, ERS Missions Section, ESA-ESRIN, 1995